Journal of Stress Analysis
Vol. 5, No. 1, Spring – Summer 2020, 69-76
Bu-Ali Sina University

ORIGINAL RESEARCH PAPER

The Effect of 2% SiO_2 Nanopowder on Mechanical Behavior of Mg AZ31

F. Barati*, M. Esfandiari, S. Babaei
Mechanical Engineering Department, Hamadan Branch, Islamic Azad University, Hamadan, Iran.

Article info

Article history:
Received 03 July 2020
Received in revised form
12 September 2020
Accepted 19 September 2020

Keywords:
AZ31 alloy
The hot ring and compression test
Bulge correction factor
Zener-Hollomon equation

Abstract

The AZ31 alloy containing nanopowder SiO_2, in comparison to other magnesium alloys, can be utilized for manufacturing extruded parts with a high loading rate. The main goal of the present study is to investigate the compressive flow stress for AZ31 alloy reinforced with 2% SiO_2 nano particles (with mean diameter of 35±2nm) in three different temperatures of 473, 493, and 513K and three strain rates of 0.0002, 0.002, and $0.02s^{-1}$ using ring compression test. The stress-strain curve at three temperatures and three strain rates were obtained by implicating the bulge and numerical correction factors. Having drawn stress and strain curve, a relation between stress and strain using the Zener-Hollomon equation, which is based on activation energy from plastic forming, was found. The coefficients of the Zener-Hollomon equation were computed for achiving the activation energy.

1. Introduction

Magnesium and its alloys in comparison to other materials have better mechanical properties such as low density, thermal conductivity, electromagnetic characteristics, high elastic modulus, etc [1-3]. The influence of correction factor and Thermo Liquid Crystal Polymer (TLCP) coreinforced on the mechanical properties of PA6-based composites were investigated and it was found that the optimum molding temperature was 240°C and the mechanical properties of the composites first increased and then decreased with an increase in TLCP content. Moreover, the introduction of a compatibilizer improved the mechanical properties of the composites [4].

Effect of metal nanoparticles on polariton dispersion in low dimensional systems was analyzed and it was found that when the percentage of Al metal nanoparticle increases, the frequency of the upper mode increases. Furthermore, the gap shifts towards longer wave vector region. The polariton dispersions at the Brillouin Zone center and the edge of $LiNbO_3/LiTaO_3$ Quantum Well, Quantum Wire, and Quantum Dot superlattice systems are studied and compared [5].

Effect of Hydrotalcite-Like compounds (HTLcs) with the high specific surface area on mechanical properties and carbonation resistance of cementitious composites were analyzed and the results showed that specific surface area of HTLcs increases with an increase in Sodium Dodecyl Sulfate (SDS) concentration, and the HTLcs have lower crystallinity when the concentration of SDS is above 0.004mmol/l. The mechanical properties of cementitious composites increase as HTLcs content vary from 0% to 1% and then decrease as HTLcs content rise from 1% to 2% [6].

The AZ31 is an Mg alloy which has been examined by many authors that are mentioned in the following.

*Corresponding author: F. Barati (Associate Professor)
E-mail address: farzanbarati@yahoo.com
http://dx.doi.org/10.22084/jrstan.2020.21334.1139
ISSN: 2588-2597

Yang and Kim studied AZ31 magnesium alloy at constant temperatures ranging from 423 to 473K. Yang and Kin mentioned that at ratios ($\sigma/G < 4 \times 10^{-3}$) and ($\sigma/G < 4 \times 10^{-3}$), the creep curves were typical class A and M behaviors, respectively. They indicated the mechanism of forming was glide-controlled dislocation creep [7].

Chung et al. investigated the fatigue and tensile properties for AZ31 and AZ61 alloys produced by Equal Channel Angular Pressing (ECAP). They stated the grain refinement of the mentioned alloys in ECAP is not dependent on fatigue strength [8]. Prasad and Rao studied processing maps on forming AZ31 in temperature range between 300-550°C by hot pressing the parallel samples to rolling direction, the normal direction, and transverse direction. The strain rate used in this study was 0.0003-0.3 1/s [9]. Kohzu et al. examined fracture mechanisms and forming limitations in cylindrical deep-drawing below 473K in AZ31 alloy. The Authors presented a remarkable improvement in ductility in AZ31 at heating between 373 to 473K [10]. Palaniswamy et al. investigated the non-isothermal (FE) simulation for forming round cups and rectangular pans from Mg alloy AZ31B sheet at room temperatures. Results of their study in terms of simulations and experiment predictions were presented. The results showed an increase in Limiting Draw Ratio (LDR) with an increase in temperature [11]. Chen and Huang [12], examined the formability of stamping for AZ31 at room temperatures by conducting various experiments. They indicated that AZ31 sheets exhibit poor formability at room temperature, but the formability is meliorated significantly at elevated temperatures. Del Valle et al., implicated electron backscattered diffraction and optical microscopy to study the microstructural evolution under tensile deformation of an AZ31 alloy with grain size ranging from 17 to 40μm [13].

Cheng et al. used the uniaxial warm tensile tests under a strain rate from 0.1-0.0001s^{-1} at a temperature range of 423-573K to predict the flow stress of AZ31 alloy sheet. The Authors indicated that the presented model by them may be a better approach at the softening stage of the flow stress in comparison to the Fields-Backofen equation [14]. Li presented a model according to three deformation modes: S (Slip), T (Twinning) and U (Untwinning), corresponding respectively to inplane tension, initial compression, and tension. They have derived a Von-Mises yield surface with initial nonzero back stress to calculate plastic yielding asymmetry [15]. Nguyen et al. [16], presented a computationally effective constitutive model which is suggested to estimate the mechanical behavior of Mg alloy sheets. The mentioned material model was implemented as a userdefined material subroutine in the commercial FE code PAM-STAMP®. Barati implicated a new numerical approach for determination of flow curve and evaluation of frictional behavior of AZ61 alloy under elevated temperature with the ring compression test [17]. Barati considered strain rarte effects on the frictional propertis of AZ61 alloy as well [17]. Sharma et al. [18] produced a hybrid nano composite consisted of grapheme, multi wall carbon nano tubes, and AZ31 alloy. They used strir friction factor method for producing process. The results of their experiments showed that the increase of tool rotation speeds leads to fracture toughness strength. Yan et al. [19] investigated the biodegradable behavior of Mg-Zn alloys prepared by powder metallurgy as a case study and they observed that the produced alloy is very homogenous and uniform. They concuded that fine grain size, tiny second phases and uniform distribution of elements made this alloy very unique. Additionally, they reported that this alloy can be a good corrosion protective as well. Barati et al. [20], studied the effects of SiO_2 on mechanical properties of AM60 alloy. They implicated an ultra weight via ultrasound-assisted casting. Their experimental results showed that SiO_2 nano particle leads to grain size reduction as well as strength increase for AM60 alloy. Hosseini Tabar and Barati [21] examined the effects of SiC nano particles on fatigue life of Aluminium matrix composites. They implicated a micromechanical model to analyze the fatigue properties of Al-based composite. The results obtained from their simulations showed that their presented model can properly predict fatigue life.

Haghani et al. [22] studied the mechanical property and microstructure of nanocomposite AZ31/SiC fabricated by friction stir process. They studied effects of 4, 8, 12 and 8 weight percentage of SiC on AZ31 alloy. Their results showed that 4% SiC addition made the most magnitude for ultimate stress, and by increasing the magnitude of SiC, the ultimate strength decreases respectively.

Although a large number of researchers have focused on effects of nanoparticles addition to magnesium alloy, but it seems that there is a lack of knowledge in modeling of reinforced-magnesium alloy especially at high temperature. In addition, the effects of nano SiO_2 on the hot compressive flow stress of AZ31 alloy have not been considered up to this study. All the previous work with con-sidering nano SiO_2 was performed at room temperature and the effects of forming condition were neglected.

The objective of this study is to investigate the mechanical behavior of Mg alloy AZ31 with 2% SiO_2 nanopowder at three strain rates of 0.0002, 0.002 and 0.02s^{-1} and three temperatures of 473, 493 and 513K.

2. Experimental Procedure

2.1. Preparation of Magnesium Alloy

In this study high porosity Mg, Al billet (with porosity equal to 99.24%) and Zn plate (with porosity equal to 99%) were prepared according to the conditions be-

low. It is worthy to know that for selecting 2% nano SiO_2, 4 different percentages of SiO_2 from 1%, 2%, 4%, and 8% were added to AZ31 and their effects on the strength of AZ31 at room temperature were investigated. The results showed that the maximum amount for the compressive strength were observed at 2% SiO_2 nano addition. Therefore, 2 weight percent SiO_2 was considered as the reinforcement phase during this research. In order to manufacture AZ31 alloy with 2% SiO_2 nanopowder, at first, a mixture from Al and Mg for 60min at 1014K in a low carbon-steel crucible was prepared. In this process to avoid the oxidation of its surface, a mixture from NaCl-$MgCl_2$ was confected. After 60min, Zn and 2% SiO_2 nanopowder were added to casting crucible and it was mixed for 2min. Once again the mixture was put in an electric furnace for 30min.

In the following part to provide standard testing sample, the number of cylinders to diameter and height equal to 6 and 9mm (for compression tests) was produced. Moreover, for ring compression test, the number of hollow rings with outer, inner diameter and height equal to 9, 4.5, and 3mm manufactured. In the following similar samples without nanopowder SiO_2 are prepared. SEM images of AZ31 with SiO_2 nanopowder is shown in Fig. 1. A hexagonal lattice structure of AZ31 is seen in Fig. 1 according to Refs. [10, 11, 17].

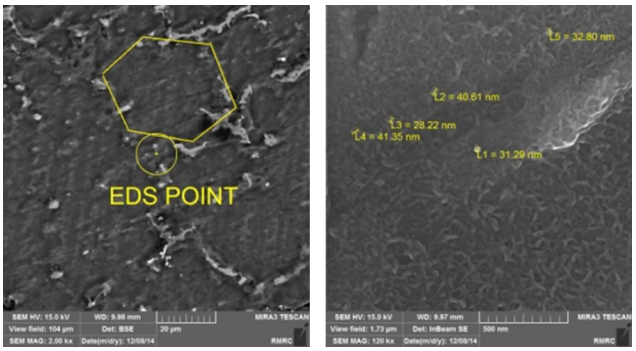

Fig. 1. SEM images of AZ31 with SiO_2 Nanopowder 10min SHT microstructure.

In the following to ensure the high porosity of Mg AZ31 with 2% SiO_2 nanopowder, a sample for EDS (Energy Dispersive X-ray Spectroscopy) testing is provided that its results are mentioned in Fig. 2. Fig.2 is the output of EDS machine that ensures us about the weight percentage of the fabricated alloy based on accelerating voltage. Fig. 3, The map of AZ31 + 2% SiO_2 , can help one to understand whether the material is homogenous or not. In addition, it is worthy to know that from the map of reinforced alloy by nanoparticles, the agglomeration can be determined as well. Maps of Mg, Al, Si, and SiO_2 are represented in Fig. 3. In this Fig. the dispersion of SiO_2 in Mg is considered homogenous.

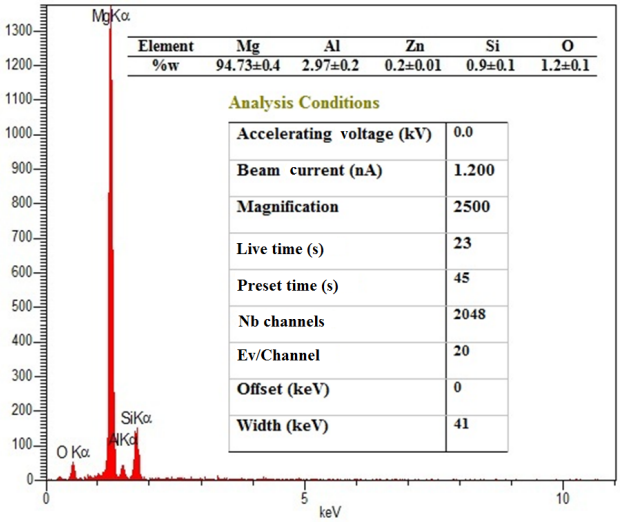

Fig. 2. The results from EDS testing on Mg AZ31 alloy with 2% SiO_2 nanopowder.

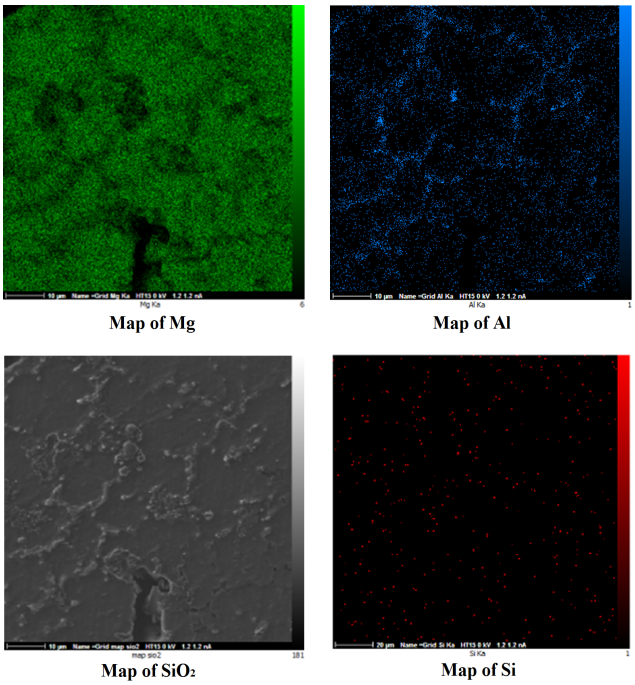

Fig. 3. Back-scattered electron compositional maps that are measured with wavelength spectroscopy.

2.2. The Hot Ring Compression Test

After preparing cylindrical (solid and hollow) samples, experimental tests with the tensile compression testing machine (15kN), (manufactured by Santam comp.) equipped with electric furnace are done. The accuracy of electric furnace is 0.1K. The hot ring and compression are carried out for three temperatures of 473, 493 and 513K, and three strain rates of 0.00025, 0.0025 and 0.025s^{-1}. In the following, the samples remained for 15min into the furnace to ensure that its temperature is constant. Accordingly, after 15min, the hot ring compression test with 8 steps and the hot compression test (with cylindrical samples) with 5 steps were done.

Totally, 72 tests for samples with/without SiO_2 at 468 steps to two repeat were performed.

In the hot ring compression test at each step, after loading, the amount of outer/inner diameter and height of samples are measured and test continues. Similarly, in the cylindrical compression test at any step, the values of height and diameter are measured. After finishing test, the sample was washed in water to prevent any further change in its microstructure. All the ring and cylindrical compression tests were done under dry interfacial conditions. In the following, the amount of flow stress and true strain can be computed.

2.3. Bulge Correction Factor

In cylindrical compression tests, barrel deformation of sample due to the presence of friction is not inconceivable. So a procedure must be presented until the dimensional variations of samples are considered. It is worth noting that in bulge correction factor, the ratio of height per diameter must be 1.5. The calculation of Bulge corrections factor is presented below. The deformed sample in the compression test is shown in Fig. 4.

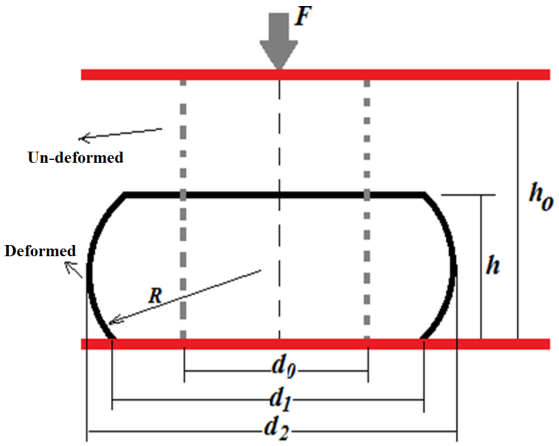

Fig. 4. The deformed sample at the compression test.

In the Bulge correction factor method, average stress and curvature radius are calculated from Eqs. (1-2) As:

$$\bar{\sigma} = \frac{4F}{\pi d_0^2} \tag{1}$$

$$R = \frac{h^2 + (d_2 - d_1)^2}{4(d_2 - d_1)} \tag{2}$$

Finally, it can be shown that C, Bulge correction factor, is computed from Eq. (3) as [17]:

$$C = \left\{ \left(1 - \frac{4R}{d_2}\right) \ln\left(1 - \frac{d_2}{4R}\right) \right\}^{-1} \tag{3}$$

In the following, stress-strain curves can be drawn by use of testing data and correction factor.

2.4. Numerical Correction Factor

The numerical correction factor is a new iterative method that correction factor can be drawn with accuracy more than previous methods such as Bulge correction factor. In this method, at first, friction coefficient using the calibration curve, drawn from the hot ring compression test, is computed. Then, the stress-strain curve drawn from bulge correction factor, and friction coefficient are inserted into finite element software (Ansys Ver. 2010). The compression testing similar to experimental procedure is modeled and eventually the modified stress-strain and force-displacement curve are drawn. Before step 2, by use of the modified stress-strain curve obtained from previous step, the calibration curve was plotted to measure friction coefficient more accurately than previous step. Having calculated the modified friction coefficient, the modified stress-strain and force-displacement curves are inserted into finite element software. The compression test is simulated and again the stress-strain and force-displacement curves are drawn. After 2 or 3 iterations, the force-displacement curve obtained from last iterations has a good agreement with force-displacement from experimental testing.

So the stress-strain curve computed from the last iterations is more accurate than the stress-strain obtained from the bulge correction factor. The numerical correction factor is accurate, especially in high strain rate loading.

3. Results and Discussion

In previous sections, enough materials to measure friction coefficient and draw the stress-strain curve at three strain rates and three temperatures were presented. Represented in Table 1 are the values of friction coefficient obtained from numerical correction factor and the hot ring compression test, at three strain rates of 0.00025, 0.0025 and 0.025s^{-1} and three temperatures of 473, 493 and 513K.

Table 1
The Friction coefficient for different temperature and strain rates.

T K	473	493	513	473	493	513
$\dot{\varepsilon}$, $[s^{-1}]$	Samples with 2% SiO_2			Samples without 2% SiO_2		
0.0002	0.30	0.33	0.37	0.31	0.34	0.37
0.002	0.28	0.32	0.37	0.28	0.33	0.37
0.02	0.26	0.30	0.33	0.26	0.31	0.34

Contrary to the previous studies, the friction coefficient is affected by temperature and strain rate, in Table 1 an increase in temperature leads to mild rise in friction coefficient. It seems that decreasing strain rates (from 0.02 to 0.0002s^{-1}) caused friction coefficient to increase. Generally, in high strain rate loading, contact time between sample and platen is lower so increasing contact time rises friction coefficient. On the other hand, increasing temperature leads to rise in internal kinetic energy, so in contact surface, the movements of molecules are grown. Based on results in Table 1, it seems that 2% SiO_2 additive does not have a considerable effect on friction coefficient. Having calculated friction coefficient using ring compression test, the amount of stress and strain by use of numerical correction method is computed.

The compressive flow stress-strain curve in $T = 473$K for different values of strain rates is shown in Fig. 5. This figure showed that strain hardening, strain softening, and steady stress-stress condition occoured for each strain rate. According to Fig. 5, it seems that an increase in strain rate from 0.0002 to 0.02 1/s leads to rise in flow stress about 61%. This phenomenon can be interpreted in this way that by decreasing the strain rates at 473K, there is a huge time for the grain for twinning process as well as dynamic recrystallization. Both twinning processs and dynamic recrystallization help to softening behavior because there is a lot of new born grains with zero stress. This zero stress grains led to decrease in the average stress and finally, the softening phenomenon occurred.

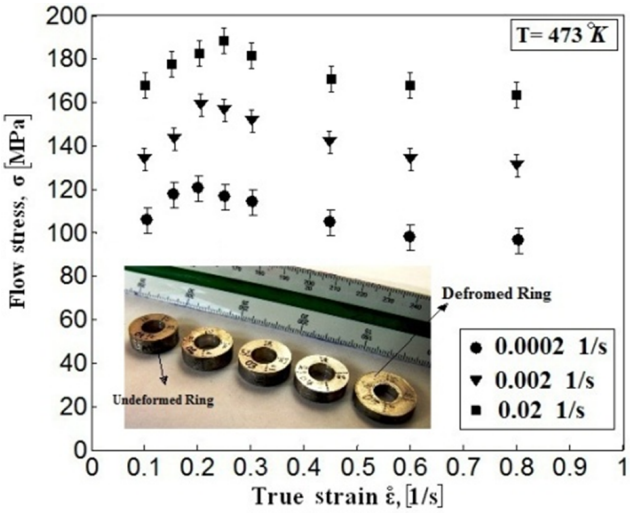

Fig. 5. The flow stress-strain curve in $T = 473$K for different values of strain rates.

The compressive flow stress-strain curve in $T = 473$K for different values of strain rates is shown in Fig. 6. Based on the result in Fig. 6, an increase in strain rate leads to increase in the ultimate flow stress which is seen in greater strain. Represented in Fig. 6 is the flow stress-strain curve for the several of strain rate in $T = 493$K. Similar to Fig. 4, with decreasing amounts of strain rate from 0.02 to 0.0002 1/s, the flow stress is reduced. The comparison between two Figs. 5-6 shows that increasing temperature caused to reduce in the flow stress of about 20%. This means that the compressive flow curve are more sensitive to temperature rather than strain rates. The increase in temperature leads to increase in the required energy for dynamic recrystallization process and twinning phenomenon. These factors help softening phenomenon act earlier at lower level of peak stresss.

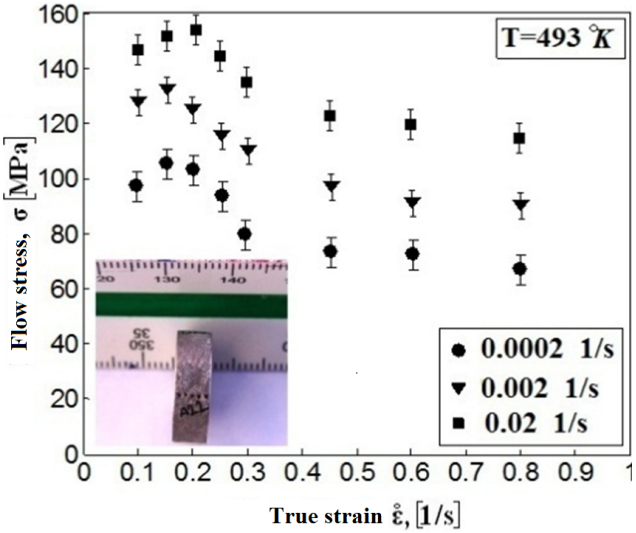

Fig. 6. The flow stress-strain curve in $T = 493$K for different values of strain rates.

The compressive flow stress-strain curve for AZ31 + 2 weight percentage of SiO_2 at $T = 513$K for different values of strain rates is shown in Fig. 7. Similar to previous Figs. 5-6, increasing temperature leads to decrease in flow stress. Based on results in Figs. 5-6, it seems those temperature and strain rates play a key role in flow stress-strain curve and with increasing temperature form 513 to 473K and reducing strain rate from 0.02 to 0.0002 1/s, the flow stress-strain curve decreases. For example, by considering strain rate equal to 0.0002 1/s and different temperature (473, 493, and 513K), the lowest compressive flow stress-strain curve occurs at the highest temperatue. This can be interpereted as the same explanation that the increase in temperature leads to increase in the required energy for dynamic recrystalization process and twinning phenomenon.

AZ31 flow curve at high temperature in various forming conditions was investigated by Fersteh-Saniee et al. [23] By comparing the results in Figs. 5-7 with AZ31 flow curve at high temperature, one can understand that adding 2% nano SiO_2 leads to increase in stress in the flow curve. These results are in accordance with Barati et al. results for AM60 alloy [20].

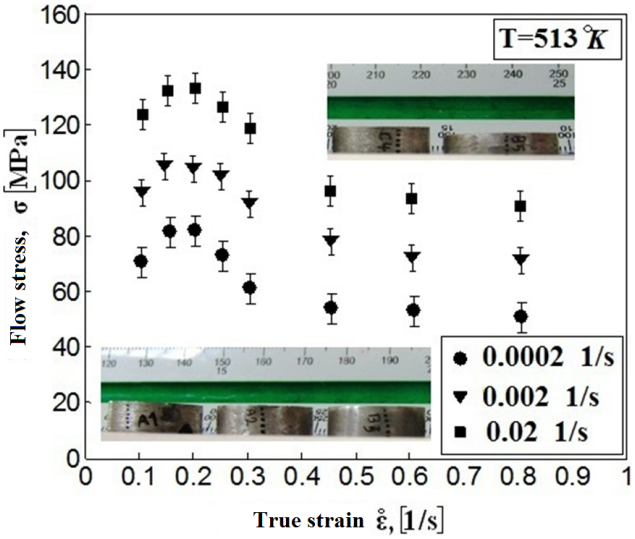

Fig. 7. The flow stress-strain curve in $T = 513$K for different values of strain rates.

In the following, an equation is presented to predict the behavior of flow stress as a function of strain, strain rate, and temperature. In this study, to estimate flow stress-strain curve, Zener-Hollomon equation is used (Eq. (3)), which is based on activation energy from plastic forming.

$$Z = \dot{\varepsilon} \exp\left(\frac{Q}{RT}\right) = A[\sinh(\alpha\sigma)]^n \tag{4}$$

In Eq. (4), Q, R, and T are activation energy in plastic forming, the gas constant, and temperature, respectively. The activation energy in temperature is calculated from Eq. (5);

$$Q = Rn\Theta \tag{5}$$

In Eq. (5), Θ and n are the slope of $\ln(\dot{\varepsilon}) - \ln(\sinh(\alpha\sigma))$ curve at constant temperature (Fig. 7) and the slope of $\ln(\sinh(\alpha\sigma)) - \{1000/T\}$ curve at constant strain and strain rate (Fig. 8), respectively. In Eqs. (4-5), α is equal to 0.055.

The curve of $\ln(\sinh(\alpha\sigma)) - \{1000/T\}$ at constant strain rate is demonstrated in Fig. 6. The relation between σ and Z can be expressed in Eq. (6);

$$\sigma = \frac{1}{\alpha} \ln\left[\left(\frac{Z}{a}\right)^{1/n} + \left(\left(\frac{Z}{a}\right)^{2/n} + 1\right)^{1/2}\right] \tag{6}$$

In the following, by use of Eqs. (4-5) and Figs. 8 and 9, the variation of Ave. activation energy as function of temperature is shown in Fig. 10.

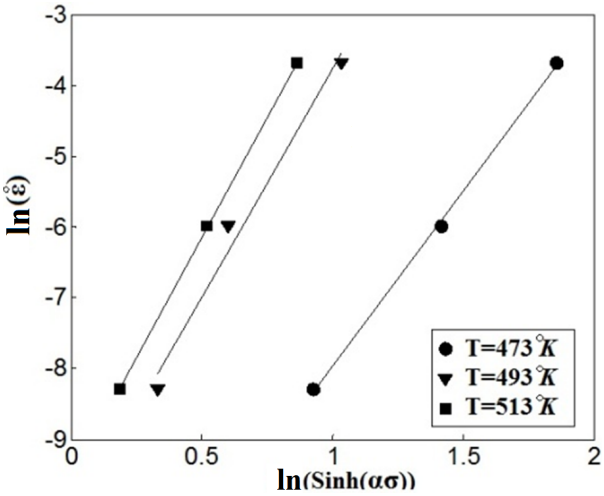

Fig. 8. The $\ln(\dot{\varepsilon}) - \ln(\sinh(\alpha\sigma))$ curve at constant temperature.

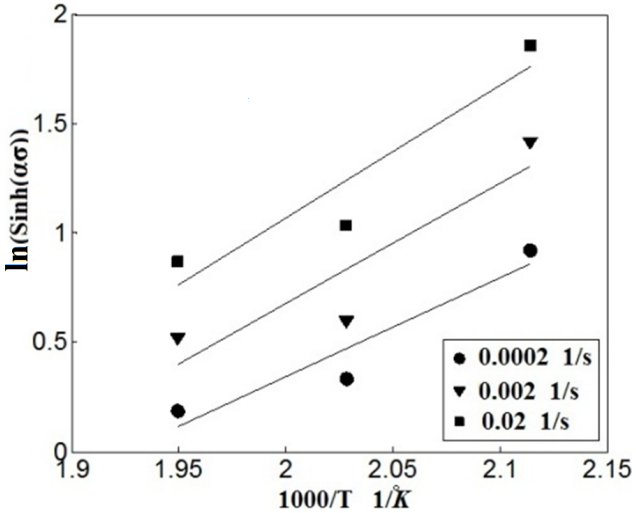

Fig. 9. The $\ln(\sinh(\alpha\sigma)) - \{1000/T\}$ curve at constant strain rate.

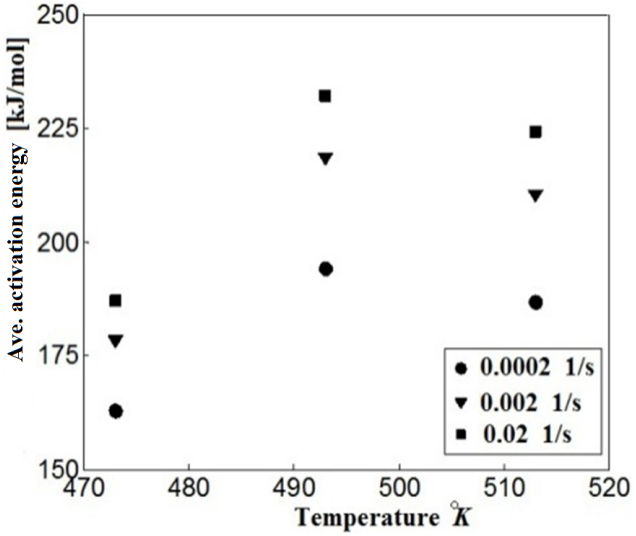

Fig. 10. The amounts of activation energy as function of temperature at constant strain rate.

In the following, by use of Eqs. (4-5) and Figs. 8-10, the $\ln(Z) - \ln(\sinh(\alpha\alpha))$ curve can be exhibited in Fig. 11.

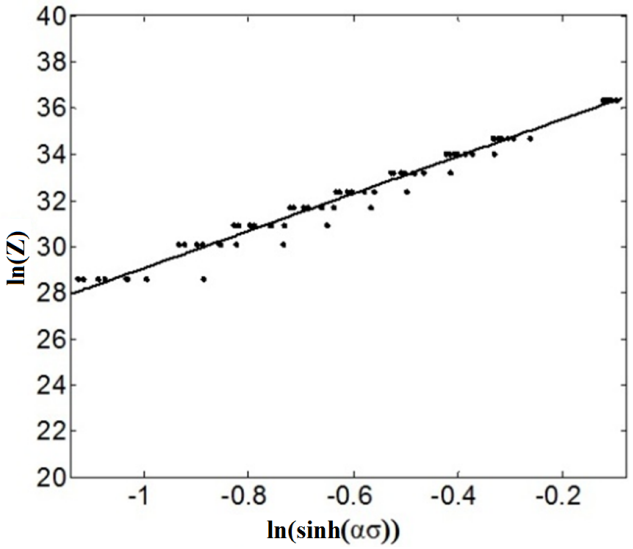

Fig. 11. The values of $\ln(Z)$ as function of $\ln(\sinh(\alpha\alpha))$.

Using Fig. 10 and Eq. (6), flow stress can be computed as function of Z (please see Eq. (4)).

4. Conclusions

Based on results in previous section, in hot forming a decrease after peak of stress is shown which is due to the new crystallization phase magnesium. Generally with increasing temperature, friction coefficient increases which is due to increase in internal energy and with decreasing strain rate, the amount of friction coefficient, due to decreasing contact time between die and samples is reduced. Increasing temperature from 473 to 493 and 513K caused the reduction of approximately 20 and 40 percent in the peak of stress, respectively.

References

[1] H. Palaniswamy, G. Ngaile, T. Altan, Finite element simulation of magnesium alloy sheet forming at elevated temperatures, J. Mater. Process. Technol., 146(1) (2004) 52-60.

[2] G. Vespa, L.W.F. Mackenzie, R. Verma, F. Zarandi, E. Essadiqi, S. Yue, The influence of the as-hot rolled microstructure on the elevated temperature mechanical properties of magnesium AZ31 sheet, Mater. Sci. Eng. A, 487(1-2) (2008) 243-250.

[3] C.E. Dreyer, W.V. Chiu, R.H. Wagoner, S.R. Agnew, Formability of a more randomly textured magnesium alloy sheet: Application of an improved warm sheet formability test, J. Mater. Process. Technol., 210 (2010) 37-47.

[4] J. Zhang, H.F. Yin, Y. Tang, H.D. Yuan, Y. Wei, Y. Hong-feng, The influence of CF and TLCP co-reinforced on the mechanical properties of PA6-based composites, Mater. Res. Express, 5(5) (2018) 121-128.

[5] V. Doni Pon, K.S.J. Wilson, Effect of metal nanoparticles on polariton dispersion in low dimensional systems, Mater. Res. Express, 6(11) (2019) 62-73.

[6] Z. Zhang, S.H. Chen, Y. Zhang, Effect of hydrotalcite-like compounds with high specific surface area on mechanical properties and carbonation resistance of cementitious composites, Mater. Res. Express, 6(11) (2019) 119-128.

[7] K.T. Yang, H.K. Kim, Elevated temperature deformation behavior in an AZ31 magnesium alloy, J. Mech. Sci. Technol., 20 (2006) 1209-1216.

[8] C.S. Chung, D.K. Chun, H.K. Kim, Fatigue properties of finegrained magnesium alloys after severe plastic deformation, J. Mech. Sci. Technol., 19 (2005) 1441-1448.

[9] Y.V.R.K. Prasad, K.P. Rao, Processing maps for hot deformation of rolled AZ31 magnesium alloy plate: anisotropy of hot workability, Mater. Sci. Eng. A, 487(1-2) (2008) 316-327.

[10] M. Kohzu, F. Yoshida, H. Somekawa, M. Yoshikawa, S. Tanabe, K. Higash, Fracture mechanism and forming Limit in deep-drawing of magnesium alloy AZ31, Mater. Trans., 42(7) (2001) 1273-1276.

[11] H. Palaniswamy, G. Ngaile, T. Altan, Finite element simulation of magnesium alloy sheet forming at elevated temperatures, J. Mater. Process. Technol., 146(1) (2004) 52-60.

[12] F.K. Chen, T.B. Huang, Formability of stamping magnesium-alloy AZ31 sheets, J. Mater. Process. Technol., 142 (2003) 643-647.

[13] J.A. del Valle, M.T. Pérez-Prado, O.A. Ruano, Deformation mechanisms responsible for the high ductility in an Mg AZ31 alloy analyzed by electron backscattered diffraction, Metall. Mater. Trans. A, 36 (2005) 1427-1438.

[14] Y.Q. Cheng, H. Zhang, Z.H. Chen, K.F. Xian, Flow stress equation of AZ31 magnesium alloy sheet during warm tensile deformation, J. Mater. Process. Technol., 208(1-3) (2008) 29-34.

[15] M. Li, Constitutive Modeling of Slip, Twinning, and Untwinning in AZ31B Magnesium, Ph.D. Thesis, Department of Materials Science and Engineering, USA: The Ohio State University, (2006).

[16] N.T. Nguyen, M.G. Lee, J.H. Kim, H.Y. Kim, A practical constitutive model for AZ31B Mg alloy sheets with the unusual stress-strain response, Finite Elem. Anal. Des., 76 (2013) 39-49.

[17] F. Barati, A numerical approach for determination of flow curve and evaluation of frictional behavior of AZ61 magnesium alloy under elevated temperature forming conditions, Measurement, 74 (2015) 1-10.

[18] S. Sharma, A. Honda, S.S. Sing, D. Verma, Influence of tool rotation speed on mechanical and morphological properties of friction stir processed nano hybrid composite of MWCNT-Grapghen-AZ 31 magnesium alloy, J. Magnesium Alloys, 7(3) (2019) 487-500.

[19] Y. Yan, X. Chu, X., Luo, X. Xu, Y. Zhang, Y.L. Dai, D. Li, L. Chen, T. Xiao, K. Yu, A homogenous microstructural Mg-based matrix model for orthopedic application with generating uniform and smooth corrosion product layerin Ringer's solution: Study on biodegradable behavior of Mg-Zn alloys prepared by powder metallurgy as a case, J. Magnesium Alloys, In Press (2020), DOI:10/1016/j.jma.2020.03.010.

[20] F. Barati, M. Latifi, E. Moayer Far, M.H. Mosallanejad, A. Saboori, Novel AM60-SiO_2 nanocomposite produced via ultrasound-assisted casting; production and characteristics, Materials, 12(23) (2019) 3976.

[21] Z. Hosseini Tabar, F. Barati, Effects of SiC particles on fatique life of Al-matrix composites, J. Stress Anal., 4(1) (2019) 73-88.

[22] A. Haghani, S.H. Noorbakhsh, M. Jahangiri, Investigation of mechanical property and microstructure of nanocomposite AZ31/SiC fabricated by friction stir process, Int. J. Adv. Des. Manuf. Technol., 9(2) (2016) 27-34.

[23] F. Fereshte-Saniee, F. Barati, H. Badnava, KH. Falah-nejad, An exponential material model for prediction of the flow curves of several AZ series magnesium alloy intension and compression, Mater. Des., 35 (2012) 1-11.